Functionally graded materials produced by laser cladding

Pei, Y.T.; Hosson, J.Th.M. De

Published in:
Acta Materialia

DOI:
10.1016/S1359-6454(00)00065-3

Publication date:
2000

PERGAMON

Acta mater. 48 (2000) 2617–2624

Acta MATERIALIA

www.elsevier.com/locate/actamat

FUNCTIONALLY GRADED MATERIALS PRODUCED BY LASER CLADDING

Y. T. PEI and J. TH. M. DE HOSSON†

Department of Applied Physics, Materials Science Center, Netherlands Institute for Metals Research, University of Groningen, Nijenborgh 4, 9747 AG Groningen, The Netherlands

(Received 1 December 1999; accepted 7 February 2000)

Abstract—AlSi40 functionally graded materials (FGMs) were produced by a *one-step* laser cladding process on cast Al-alloy substrate as a possible solution for interfacial problems often present in laser coatings. The microstructure of the FGMs consists of a large amount of silicon primary particles surrounded by α-Al dendritic halos and by Al/Si eutectic. The Si particles exhibit a continuous increase in both size and volume fraction, from 8.5 μm and 22.7% at the bottom to 52 μm and 31.4% at the top of the FGM layer, respectively. The morphology of the Si particles changes accordingly from a small polygonal shape to a coarsely branched equi-axial shape. The α-Al halos and eutectic areas show less change over the same distance. From an analysis of the temperature field of the laser pool, Si particles heterogeneously nucleate on incompletely melted Si particles. The number density of Si particles is most likely being controlled by the non-homogeneous temperature field of the pool that determines the decomposition of the original Si phase in the AlSi40 powder. The growth rate and time available at different depths of the laser pool mainly affect the final size of Si particles.

Keywords: Functionally graded materials; Aluminum alloy; Laser coating; Microstructure; Solidification

1. INTRODUCTION

Laser surface processing of aluminum alloys has attracted considerable interest to enhance the mechanical and chemical resistance of Al-alloy components [1]. Examples of laser surface processing techniques include laser transformation [2], surface melting (LSM) [3], laser surface alloying (LSA) [4–6] and laser surface cladding (LSC) [7]. In the case of LSM, the surface performance of the Al-alloy substrate is modified mainly by the homogenization and refinement of the microstructure. In addition, different precipitates may be formed and the supersaturation of the α-Al phase increased due to non-equilibrium solidification [8–10]. However, the modification is limited because the composition of the melted layer is the same with respect to the substrate and substantial tensile stresses may be generated [11–13]. The employment of appropriate alloying additions with LSA can lead to the formation of hard phases that reinforce and enhance the properties of the alloyed layer [14–16]. Elements used to date have been restricted to the transition metals such as Ni, Cr, Mo, W, Ti and Zr that react with Al forming intermetallic aluminides [1]. The LSA technique works on the principle of mixing of the alloying element in the melt pool of the substrate created by the laser beam. The amount of alloying addition is usually minor compared with the total amount of molten material. Therefore, local thermal distortions may be introduced to the substrate resulting in severe residual stresses.

Previous studies [17, 18] have shown that LSC is an appropriate technique. In this process only a thin surface layer of Al-alloy substrate melts together with the additive material to form a coating. By minimizing the thickness of the melted substrate layer, the desired properties of the coating are realized while minimizing the changes to the substrate. Consequently, advanced coatings produced by LSC can be designed independent of the composition of the substrate material. Therefore, LSC has the potential to be an efficient and cost-effective technique to improve the surface properties with the ability of significantly extending the performance of the material as a whole.

Nevertheless, a major drawback in laser cladding is the commonly observed bad wetting behavior of the metal/ceramic system [19–21]. In addition between the coating and the substrate a sharp interface usually forms that is often a potential source

† To whom all correspondence should be addressed.

1359-6454/00/$20.00
PII: S1359-6454(00)00065-3

of weakness. For example, if the coating material has a very different thermal expansion coefficient to the substrate, there is the possibility of severe stress build-up at the interface and crack propagation may result. A common way to circumvent this problem is to optimize the thickness of the coating or to introduce a compliant interlayer for the reduction of the thermal stress. Unfortunately, most compliant films also melt at lower temperature. A recent development by Jasim *et al.* [22] is a functionally graded material built up by three overlaid laser tracks in which the fraction of SiC reinforcement increased in steps from 10 to 50 vol.%. Their work showed the possibility of laser processing to deposit a thick multi-layer of essentially discrete composition rather than a gradual change in composition.

The term of "functionally graded materials" (FGMs) is now widely used by the materials community for a class of materials exhibiting spatially inhomogeneous microstructures and properties [23]. Graded materials in themselves are not something new, but what is exciting about them is the realization that gradients can be designed at a microstructural level to tailor specific materials for their functional performance in particular applications. Therefore, a possible approach for eliminating the sharp interface present in LSC is to introduce the concept of FGMs into the design of coating structure. This paper reports on the exploration of the laser cladding technique, in which a progressive change in both microstructure and related properties is achieved over the molten boundary of the laser pool in such a way that interfacial problems are being solved.

2. EXPERIMENTAL DETAILS

Aluminum-based substrates were cut from cast rods of a commercial alloy with a nominal composition (wt%): 6.3Si, 0.3Mg, 1.0Fe, 4.0Cu and Al in balance. Standard face milling finished the surfaces of the flat substrate specimens in dimensions of $100 \times 50 \times 10\ mm^3$. The specimen was mounted on a cooling block with the underside in direct contact with flowing water or oil maintained at a constant temperature. In this way the substrate was kept at a constant temperature as much as possible with a change of less than 5°C during laser cladding. This ensured that the geometry and dilution degree of laser clad tracks depended only on the processing parameters. In addition, applying different substrate temperatures, i.e. from 15 to 200°C, made it possible to adjust the thermal gradient of the specimens that affected the solidification of the laser pool.

AlSi40 alloy powder was used as coating material for the following reasons. Firstly, the use of the same Al-based system results in similar thermal properties. Secondly, even a high degree of local dilution can create a composition gradient for the desired FGMs. Finally, the primary Si particles may serve as hard reinforcements to FGMs and the solidification process can control their size. This is very important for the *in situ* formation of FGMs during laser cladding. The powder produced with spray-atomizing technology exhibited a globular geometry with particle size of 50–125 μm as shown in Fig. 1.

The powder feeder used was a Perkin-Elmer-Metco Co. (MFP-I type) commercial instrument. The cladding setup was equipped with a specially developed powder addition module [24]. The powder nozzle had an integrated coaxial shielding gas flow to buffer the laser molten pool from the atmosphere. The shielding gas was also used to converge and to concentrate the powder stream into the laser molten pool, leading to a powder yield factor Y close to unity as well as a more homogeneous cladding track with a smooth surface. The yield factor being equal to unity if no powder is blown aside or evaporates, is high when the proper operating conditions are used.

In this work a HAAS HL3006D-type 3 kW Nd:YAG laser was used. The laser beam was transported by means of a ⌀ 0.6 mm fiber, resulting in a homogeneous intensity distribution. The focal length of the focusing lens was 140 mm. It was operated at 25 mm defocusing distance with a ⌀ 3.34 mm spot on the surface of the substrate for cladding. A numerically controlled four-axial machine executed the specimen movement. The processing parameters varied in the range of 2000–3000 W laser power, 8.3–26.7 mm/s beam speed and 10–30 g/m powder feed rate. The shielding gas was helium with a flow rate of 0.167 l/s.

The transverse sections of the clad tracks were cut for microstructural examinations. A Philips XL-30 FEG scanning electron microscope (SEM)

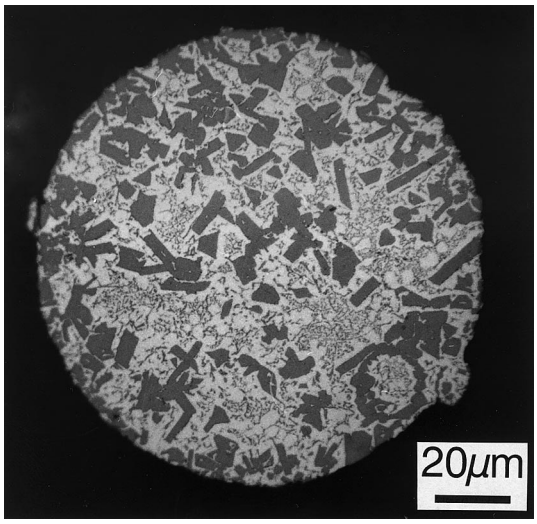

Fig. 1. Optical micrograph of AlSi40 powder showing the original Si primary particles inside the powder.

equipped with energy disperse X-ray analysis (EDAX) and a standard optical microscope were employed for the microstructure study. The samples were etched with 2% NaOH solution for 5–10 s at 40°C. A Shimadzu HMV-2000 type micro Vickers was used for hardness measurements. The load used was 200 g and loading time was set at 15 s. An average value of hardness was taken from five to eight measurements executed at the same depth on three different cross sections of a FGM track.

3. RESULTS

Figure 2 presents the cross sections of laser clad single AlSi40 FGM tracks produced by different beam speeds. All of the tracks exhibited a good fusion bond with the substrate. Within the substrate there are casting defects in the form of large voids. If the melt boundary of the laser pool reached the voids, then the trapped gases of the voids were brought into the melt. Consequently some pores indicated by arrows in Fig. 2(c) appear in the clad layer produced at higher beam velocity, because the gas bubbles did not have enough time to escape from the melt. However, the FGM tracks are always porosity free if there was not a void inside the melted layer of the substrate.

A large amount of primary Si particles (Si_p) are observed over the whole cross sections of FGM tracks. These fine Si particles act as reinforcement and are expected to improve the tribological properties of the FGMs significantly. Note that the pri-

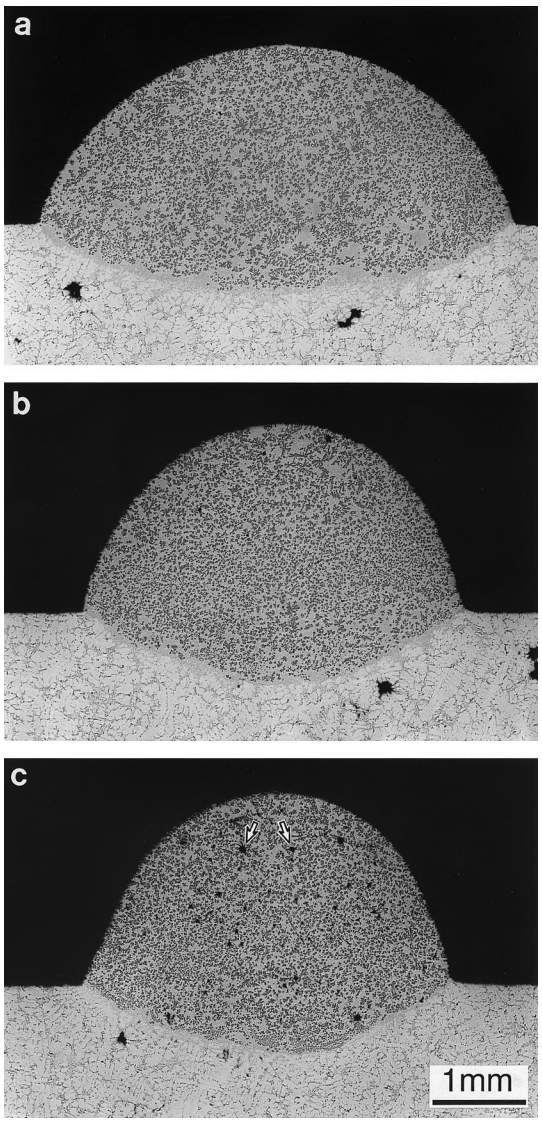

Fig. 2. Optical micrographs of AlSi40 FGMs clad at 3000 W laser power and different beam speeds of: (a) 10 mm/s; (b) 20 mm/s; (c) 26.7 mm/s. The arrows indicate some pores.

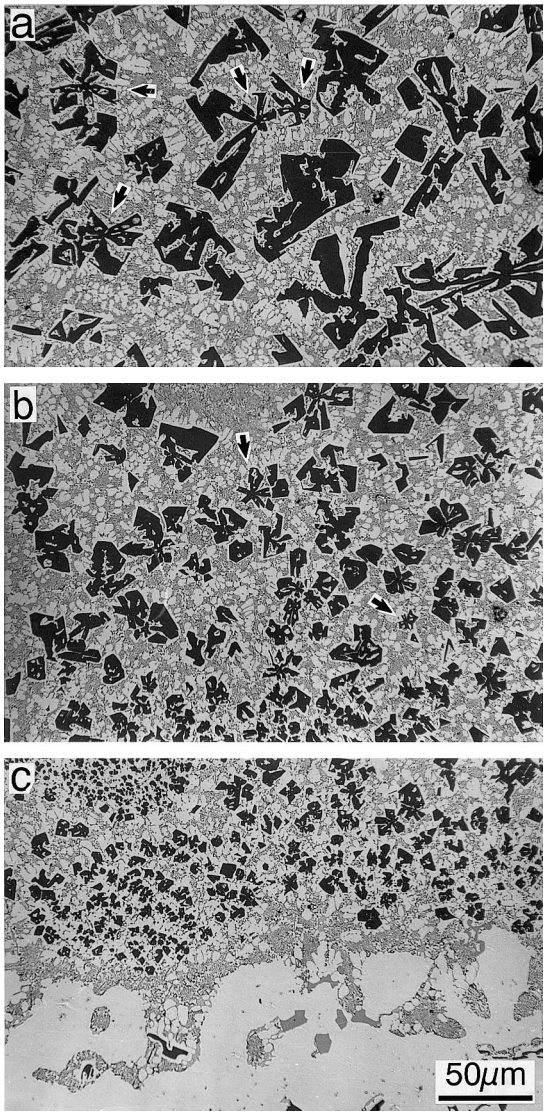

Fig. 3. Graded microstructure of AlSi40 FGM produced at 3000 W laser power and 26.7 mm/s beam speed: (a) at top part; (b) at intermediate part; (c) at bottom. (All the arrows indicate five-branch Si particles.)

mary Si particles gradually increase in size with distance from the bottom of FGM tracks. Moreover, the scanning speed of the laser beam exerts an obvious influence on the distribution of Si particles. The difference in Si_p size between the top and the bottom of the tracks decreases with decreasing beam speed.

The graded microstructure of AlSi40 FGM is more clearly revealed in Fig. 3. The FGM layer consists of primary Si crystals surrounded by α-Al dendritic halos and branched Al/Si eutectic adjacent to the α-Al halos. From the bottom to the top surface of the clad FGM layer, the discrete Si particles increase in apparent size by a factor of six (from 8.5 ± 1.1 to 52 ± 2.7 μm). In contrast, the α-Al halos and the adjacent eutectic cells exhibit less change in size over the same distance. These observations suggest that the primary silicon particles were nucleated from the liquid state rather than from a solid state precipitate. In addition, a thin Si_p-free zone composed of α-Al dendrites and Al/Si eutectic can be seen at the melted boundary. The thickness of this Si_p-free zone reduces from 30 to 10 μm with increasing beam speed. It is predicted that this zone will be a beneficial feature by being a region where possible thermal stresses may be relieved.

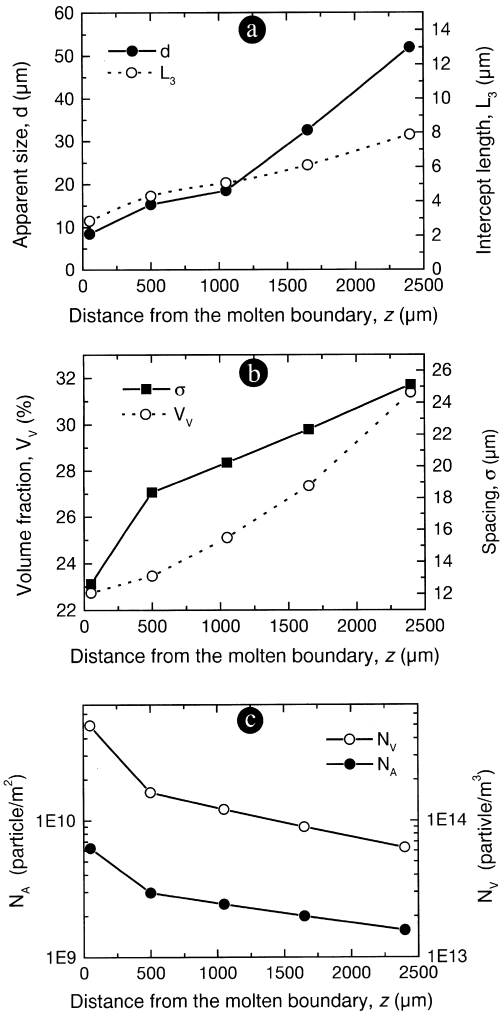

Fig. 4. Quantitative metallography results of the FGM track revealed in Fig. 3 on the graded change of Si particles as a function of depth about: (a) apparent size and mean intercept length; (b) volume fraction and interparticle spacing; (c) area density N_A and volumetric density N_V.

The changes in apparent size, volume fraction and number density of Si particles as a function of the distance (z) from the molten boundary are displayed in Fig. 4 based on quantitative metallographic analysis. The size of the Si particles is evaluated in Fig. 4(a) in two terms, i.e. an apparent size (d) and a mean intercept length (L_3). The apparent size of the Si_p is taken as the tip-to-tip distance of the star-shaped particles and represents the maximum distance of growth for a particle along certain preferred directions. The mean intercept length denotes the average size of particles and is a unique assumption-free value that is valid for particles of any size and configuration. Both parameters exhibit an obvious increase over the thickness of the FGM, i.e. six times in d and 2.7 times in L_3, and their difference is due to the development in shape of Si_p. Accordingly, the volume fraction of Si_p varies continuously from $22.7\pm0.64\%$ at the bottom to $31.4\pm0.92\%$ at the top of the track, see Fig. 4(b). Note that the numbers of Si_p observed per unit area and subsequently calculated per unit of volume decreases clearly with z as is shown in Fig. 4(c). In other words, the interparticle spacing (σ) increases significantly with z and the following empirical relationship was found:

$$\sigma = 12.97 + 8.83 \times 10^{-2} z - 1.63 \times 10^{-6} z^2 \qquad (1)$$

by polynomial regression of the profile present in Fig. 4(b).

In addition to the change in size with depth, Si particles also display a morphological transition from a polygon at the bottom to an equi-axially branched shape at the top region of the FGM. An example of the equi-axially branched shape can be seen as the five-fold branched grains indicated by arrows in Fig. 3. Such five-fold geometry of Si crystals has been previously reported as a rare morphology that forms at slow cooling rate [25], but in our case it seems to be very often observed in the upper region of the FGM. It has been known that they grow from a twinned decahedral nucleus, which is an assembly of five silicon tetrahedrons in a twin orientation. The typical growing feature of the five-fold Si particles is shown in Fig. 5. The obtuse facet angles at the ends of each branch, as well as the twin planes along the branches and through the intersection points of the facets, suggests a twin plane re-entrant edge (TPRE) growth mechanism [26].

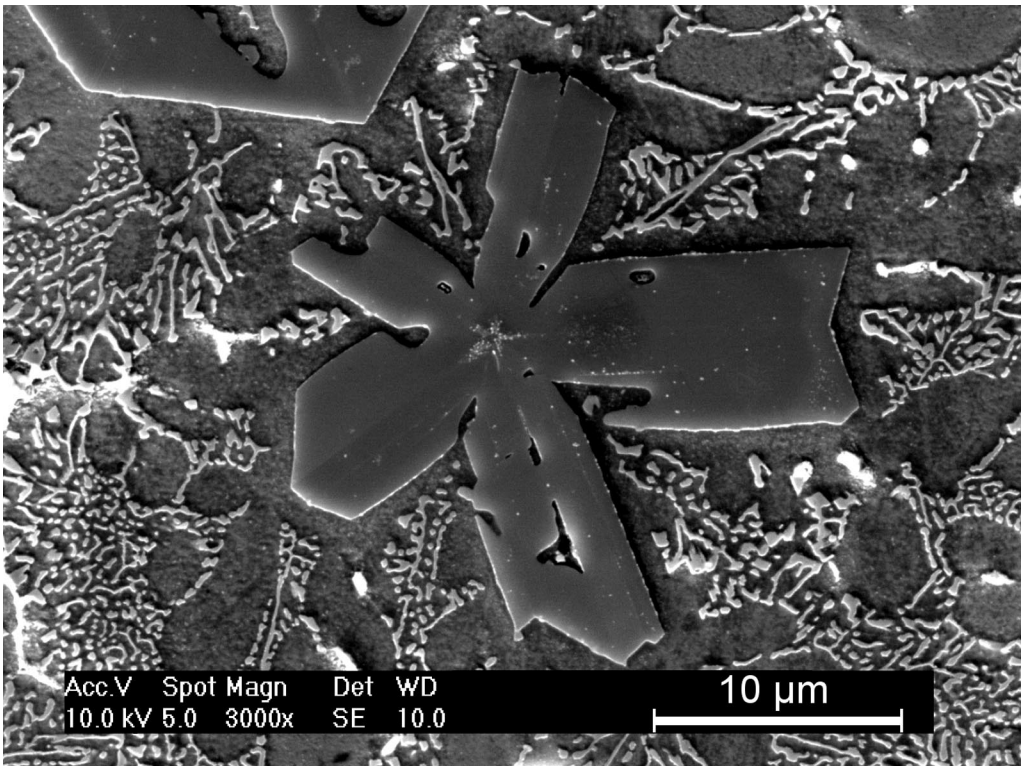

Fig. 5. SEM micrograph showing the growth feature of the five-branch Si particle and the surrounding α-Al dendritic halos as well as the eutectic adjacent to α-Al.

A typical hardness profile of the FGM tracks is presented in Fig. 6. The graded microstructure leads to a gradual hardness distribution of the FGM, from $HV_{0.2}$ 180 down to $HV_{0.2}$ 80. Sometimes it was impossible to avoid making indentations close to the primary Si particles, the result of which is a much higher hardness. This resulted in some fluctuations on the hardness curves, despite that an average of five measurements was taken. It is interesting to note that the transition from the coatings to their substrate exhibits a gradual change in the hardness, which indicates an absence of a sharp demarcation in materials properties across the interface.

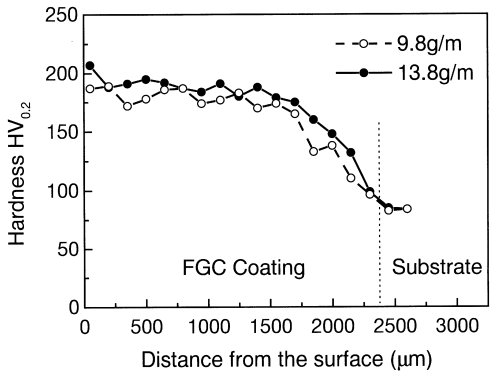

Fig. 6. Hardness distribution of laser clad AlSi40 FGMs produced with different powder feed rates.

4. DISCUSSION

The graded microstructure of AlSi40 FGM is formed during the solidification of the laser pool. Therefore, factors that affect the nucleation and growth of Si particles and of α-Al halos will play a role in controlling the formation of the graded structure. The observed microstructures suggest the following description of the solidification process of AlSi40 FGMs: the Si particles nucleate from the liquid by a heterogeneous mechanism and grow into the undercooled melt of the surroundings and reject the aluminum solvent until the local concentration is sufficient to nucleate α-Al phase. This α-Al phase appears as halos surrounding the Si particles, which arrest the growth of Si particles. The growth of the α-Al halos results in an increasing Si content of the remaining liquid phase to the extent that eventually the composition of the liquid phase lies in the coupled zone. This results in the cooperative growth mechanism between Si and α-Al that yields the eutectic phase in the latter stages of solidification. The gradual change in size and morphology of Si_p as well as α-Al halos is a consequence of their local growth conditions and nucleation environments.

4.1. Growth rate of Si particles

During laser cladding at constant power and laser beam velocity, a steady-state melt pool is created after the first few millimeters of the track. Taking a longitudinal section through the centerline of the track, the speed of the solidification front, V_s, is correlated to the beam speed, V_b, via the expression [8]

$$V_s = V_b \cdot \cos\theta \tag{2}$$

where θ is the angle between V_s and V_b, see Fig. 7. This equation is based on geometrical considerations of the melt pool, that is to say the motion rate of its isotherms follows exactly the beam velocity. V_s varies from zero at the bottom of the melt pool to a maximum approaching the value of V_b at the top of the melt pool. In the case of laser cladding AlSi40 FGMs that involve the formation of primary particles ahead of the solidification front, V_s represents the speed of the eutectic growth front, rather than the growth rate of the Si particles and of the α-Al halos. This is different compared with the case of epitaxial regrowth from a substrate during laser remelting. Although it is difficult to know the actual value of the Si_p growth rate (V_s^{Si}), it can be expected to take a similar trend with depth comparable to V_s of the eutectic, as required by the steady-state movement of the laser pool. For a given velocity of the track, relating the number of Si_p observed at different depths to the estimated V_s^{Si}, suggests that the Si_p number density decreases with increasing growth front speed. This differs from the results reported by Gremaud *et al.* [27] and contradicts classical solidification theory. Generally, for faster solidification rates more particles nucleate. This is related to the undercooling, ΔT, via the following two equations [28]:

$$N_V = N_V^0 \exp(\beta \Delta T) \tag{3}$$

and

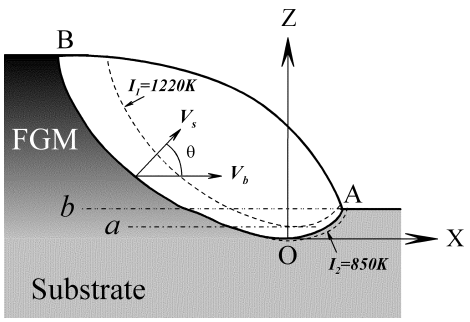

Fig. 7. Temperature field of the laser pool in the case of cladding AlSi40 FGMs: isotherms I_1 and I_2 represent the liquidus of AlSi40 alloy and the Al/Si eutectic temperature, respectively, V_b the laser beam velocity and V_s the velocity of the eutectic growth front.

$$\Delta T = K v^{\alpha} \tag{4}$$

where N_V represents the volumetric density of particles and v is the growth rate, N_V^0, β, K and α are all positive constants with $\alpha = 0.25$–0.5 depending on the actual growth mechanism. Therefore, in our case additional factors appear to affect the microstructure after solidification.

4.2. Temperature field of laser pool and nucleation density of Si particles

To understand the formation of the graded microstructure, it is necessary to know the temperature field of the melt pool in which the AlSi40 powder is melted together with the surface layer of the substrate. Following the numerical model for laser cladding created by Hoadley and Rappaz [29], the temperature field of the laser pool in the case of clad AlSi40 FGMs may be described as in Fig. 7. It is composed of two isotherms I_1 and I_2 that represent the liquidus of the AlSi40 alloy (1220 K) and the eutectic temperature of Al–Si alloy (850 K), respectively. The molten region of the boundary of the pool (i.e. denoted as line OA) corresponds to the liquidus of the Al-alloy substrate (about 900 K). The pool is divided into three parts by drawing two horizontal lines, *a*, as a tangent to the lowest point of the isotherm I_1 and, *b* coincides with the surface of the substrate. The part of the pool above line b is in a superheated condition, i.e. the temperature of the liquid exceeds the liquidus temperature (1220 K). Evidence in support of this was given by optical pyrometer measurements of the mean surface temperature of the melt and it was found that the temperature of a 2 mm diameter area of the melt pool surface was 1650–1800 K. The temperature of the melt below line *a* never exceeds the liquidus of AlSi40 alloy and cools down quickly to the liquidus temperature of the substrate alloy due to mixing of the melt. In this region of the melt it is expected that the decomposition of the original Si primary particles from the AlSi40 powder is incomplete due to premature mixing with the relatively cool melt from the substrate. Consequently, there would be many particles of Si available that are above the critical size for heterogeneous nucleation and which become active sites for growth. By decreasing the laser beam velocity, the dissolution of the original Si primary particles from the AlSi40 powder is more complete and therefore, the number density of these incompletely melted Si particles decreases as shown in Fig. 2. However, there will be fewer Si particles inside the superheated melt behind the isotherm I_1 in the upper region of the melt pool such that fewer particles can obtain the critical size for continued growth. The portion between lines *a* and *b* can be considered a transient region and presents a gradual increase both in temperature and in number of Si particles. It can be assumed that the

final number of Si particles observed in a particular part of the track is similar to the original number of incompletely melted Si particles in the melt. The observed variation of Si_p number density [$0.63–4.95 \times 10^{14}$ Si_p/m^3 shown in Fig. 4(c)] over the whole cross section of the FGM supports the above hypothesis of heterogeneous nucleation on the incompletely melted particles as it is too low for a homogeneous nucleation mechanism.

4.3. Growth time of Si particles

The primary Si particles nucleate and grow within the undercooled melt ahead of the main solidification interface and continue to grow as long as the imposed local undercooling permits. The latent heat that is released makes the solidified Si particles somewhat hotter than the surrounding liquid and establishes a negative thermal gradient around the Si particles. This leads to difficulties in determining the amount of local undercooling at different depths in the laser pool and therefore, in relating the growing rate of Si crystals to the degree of undercooling. Nevertheless, it is possible in this case to estimate the amount of time available for Si_p to grow before the α-Al halos nucleate. From the above discussion, Si_p must nucleate ahead of the eutectic interface at a distance about the same as the interval between two isotherms, which is proportional to the mean particle interspacing σ. Therefore, the growing time (t) for Si_p can be estimated by the expression

$$t = \varphi\sigma/V_b \tag{5}$$

where φ is a proportionality factor of the interval between the isotherms to the Si_p interspacing. This factor is larger than unity and can be affected by the geometry of the clad tracks or by the heat conducting condition. The studies of Gremaud *et al.* [27] assumed that during the laser remelting process of Al–26 wt% Si the primary Si particles nucleated ahead of the eutectic interface at a distance approximately equal to the average particle spacing, which means φ is unity. Their assumption is not appropriate to explain our results. Because Si particles nucleate at a temperature below the liquidus (1220 K) of AlSi40, for the observed maximum average particle spacing of 40 μm in AlSi40 FGMs the thermal gradient between two isotherms will reach 9250 K/mm. Such a large thermal gradient seems to be unlikely for a thick laser clad AlSi FGM on an Al-alloy substrate. Taking a 2 mm thick AlSi40 FGM, the maximum surface temperature measured is never greater than 2000 K. Assuming that the temperature at the molten boundary of the laser pool takes the liquidus temperature (900 K) of the substrate, the average thermal gradient over the whole pool is less than 1000 K/mm. It is reasonable to expect that the interval between the isotherms is proportional to but larger than the particle spacing. This proportional factor is represented by φ in equation (5) and is assumed to be constant with depth. The reason for using V_b rather than V_s in equation (5) is to consider a steady movement of the laser pool. By substitution of equation (1) into equation (5), the growth time can be found. Herewith it follows that the Si particles in the upper region of the melt have a significantly longer time for growth than those particles at the bottom of the track. Hence, the Si particles in the upper region of the melt are bigger.

4.4. Formation of Al halos

The liquid phase surrounding the Si particles becomes enriched with aluminum by the growth of the Si particles, which involves rejection of aluminum solute. As described by Barclay *et al.* [30], the liquid composition moves down along the depressed liquidus, passes the coupled zone and proceeds to the hypoeutectic side. Once the undercooling at the solid–liquid interface is large enough, α-Al will nucleate on the facets of the Si crystals and consequently, the growth of the latter is halted. As can be seen in Fig. 3 the α-Al halos surrounding the Si_p in the lower part of the track are thinner than those in the upper part. Another notable feature is that the dendritic nature of the α-Al halos is more fully developed further from the bottom of the track. This is considered to be additional evidence that their growth rate increases with decreasing depth in the melt pool. These observed characteristics suggest that the size of the halos is limited by both their growth rate and by the time necessary to reach the temperature at which the eutectic finally forms. Obviously, because of the smaller thermal gradient, the halos in the upper part have a greater amount of time to grow. In addition, the impingement between the Si particles relatively close to each other in the lower part restricts the halos from developing fully.

5. CONCLUSIONS

The main conclusions of our work are the following:

1. Using a *one-step* laser powder cladding process, AlSi40 functionally graded coatings (FGMs) can be obtained that consist of silicon primary particles surrounded by α-Al dendritic halos and, in turn, by Al/Si eutectic.
2. The Si particles exhibit a continuous increase in both size and volume fraction from the bottom to the top of the FGM tracks. The morphology of the Si particles also changes correspondingly from small polygons to a coarsely branched equiaxial shape from the bottom to the top of the FGM tracks. The α-Al halos and eutectic show

fewer changes over the same distance.

3. From a qualitative analysis of the temperature field of the laser pool, Si particles heterogeneously appear to nucleate on incompletely melted Si particles. The number density of Si particles is most likely controlled by the non-homogeneous temperature field of the pool that determines the decomposition of the original Si phase in AlSi40 powder. The growth rate and time available at different depths of the laser pool mainly affect the final size of Si particles.

Acknowledgements—The Netherlands Institute for Metals Research and the Foundation for Fundamental Research on Matter (FOM-Utrecht) are acknowledged for their financial support.

REFERENCES

1. Watkins, K. G., McMahon, M. A. and Steen, W. M., *Mater. Sci. Engng*, 1997, **A231**, 55.
2. Hegge, H. J., De Beurs, H., Noordhuis, J. and De Hosson, J. Th. M., *Metall. Trans.*, 1990, **21A**(4), 987.
3. Hegge, H. J. and De Hosson, J. Th. M., *Acta metall.*, 1990, **38**, 2471.
4. Kloosterman, A. B., Kooi, B. J. and De Hosson, J. Th. M., *Acta mater.*, 1998, **46**, 6205.
5. Kooi, B. J., Kabel, M., Kloosterman, A. B. and De Hosson, J. Th. M., *Acta mater.*, 1999, **47**, 3105.
6. De Mol van Otterloo, J. L. and De Hosson, J. Th. M., *Acta mater.*, 1997, **45**, 1225.
7. De Hosson, J. Th. M., in *Intermetallic and Ceramic Coatings*, ed. N. B. Dahotre and T. S. Sudarshan. Marcel Dekker, New York, 1999, p. 307.
8. Gremaud, M., Carrard, M. and Kurz, W., *Acta metall. mater.*, 1990, **38**, 2587.
9. De Mol van Otterloo, J. L., Bagnoli, D. and De Hosson, J. Th. M., *Acta metall. mater.*, 1995, **43**, 2649.
10. Noordhuis, J. and De Hosson, J. Th. M., *Acta metall. mater.*, 1993, **41**, 1989.
11. De Hosson, J. Th. M., De Mol van Otterloo, J. L. and Noordhuis, J., in *Laser Processing: Surface Treatment and Films Deposition*, ed. J. Mazumder, O. Conde, R. Villar and W. M. Steen, *NATO ASI Series E*, Vol. 307. Kluwer Academic, Dordrecht, 1996, pp. 491 and 511.
12. Noordhuis, J. and De Hosson, J. Th. M., *Acta metall. mater.*, 1992, **40**, 3317.
13. De Beurs, H. and De Hosson, J. Th. M., *Appl. Phys. Lett.*, 1988, **53**, 663.
14. Almeida, A., Anjos, M., Vilar, R., Li, R., Ferreira, M. G. S., Steen, W. M. and Watkins, K. G., *Surf. Coat. Technol.*, 1995, **70**, 221.
15. Hegge, H. J. and De Hosson, J. Th. M., *J. Mater. Sci.*, 1991, **26**, 711.
16. McMahon, M. A., Watkins, K. G., Steen, W. M., Villar, R. and Ferreira, M. G. S., in *Laser Processing: Surface Treatment and Films Deposition*, ed. J. Mazumder, O. Conde, R. Villar and W. M. Steen, *NATO ASI Series E*, Vol. 307. Kluwer Academic, Dordrecht, 1996, p. 337.
17. Sallamand, P. and Pelletier, J. M., *Mater. Sci. Engng*, 1993, **A171**, 263.
18. Liu, Y., Mazumder, J. and Shibata, K., *Metall. Mater. Trans.*, 1994, **25B**, 749.
19. Zhou, X. B. and De Hosson, J. Th. M., *Acta mater.*, 1996, **44**, 421.
20. Zhou, X. B. and De Hosson, J. Th. M., *Acta metall. mater.*, 1994, **42**, 1155.
21. Zhou, X. B. and De Hosson, J. Th. M., *Acta metall. mater.*, 1991, **39**, 2267.
22. Jasim, K. M., Rawlings, R. D. and West, D. R. F., *J. Mater. Sci.*, 1993, **28**, 2820.
23. Shiota, I. and Miyamoto, Y. (ed.), *Functionally Graded Materials*. Elsevier, Amsterdam, 1997.
24. Volz, R., Reichelt, U., Wolf, S., Pei, Y. T. and Zuo, T. C., in *Proc. 30th ISATA: Rapid Prototyping/Laser Applications in the Automotive Industries*, ed. D. Roller. Automotive Automation Ltd, Croydon, England, 1997, p. 393.
25. Kobayashi, K. and Hogan, L. M., *Phil. Mag. A*, 1979, **40**, 399.
26. Flemings, M. C., in *Solidification Processing*. McGraw-Hill, New York, 1974, p. 319.
27. Gremaud, M., Allen, D. R., Rappaz, M. and Perepezko, J. H., *Acta metall. mater.*, 1996, **44**, 2669.
28. Turnbull, D., *Acta metall.*, 1953, **1**, 8.
29. Hoadley, A. F. A. and Rappaz, M., *Metall. Trans.*, 1992, **23B**, 631.
30. Barclay, R. S., Niessen, P. and Kerr, H. W., *J. Cryst. Growth*, 1973, **20**, 175.